Development of an Organ-on-a-Chip for Correlative Microscopy: Visualizing Early Osteogenesis in 3D with High Resolution

Judith M. Schaart, Dorothee Wasserberg, Marcos A. Eufrásio Cruz, Mariska Kea-te Lindert, Robin H.M. van der Meijden, Rona Roverts, Nataliya D. Debera, Minh Phu Lu, Jeroen Rouwkema, Wouter H. Nijhuis, Andries D. van der Meer, Pascal Jonkheijm, Nico Sommerdijk*, Anat Akiva**

J.M. Schaart, M. Kea-te Lindert, M.A. Eufrásio Cruz, R.H.M. van der Meijden, R. Roverts, N. Sommerdijk, A. Akiva
Department of Medical BioSciences, Radboud University Medical Center, Geert Grooteplein Zuid 28, 6525 GA Nijmegen, The Netherlands
E-mail: anat.akiva@radboudumc.nl nico.sommerdijk@radboudumc.nl

M. Kea-te Lindert, M.A. Eufrásio Cruz, R.H.M. van der Meijden, R. Roverts, N. Sommerdijk, A. Akiva
Electron Microscopy Center, Radboudumc Technology Center Microscopy, Radboud University Medical Center, Geert Grooteplein Noord 29, 6525 EZ Nijmegen, The Netherlands

D. Wasserberg, N.D. Debera, M.P. Lu, P. Jonkheijm
Department of Molecules and Materials, Laboratory of Biointerface Chemistry, Organ-on-Chip Centre, TechMed Centre and MESA+ Institute, University of Twente, Drienerlolaan 5, 7522NB Enschede, The Netherlands
E-mail: p.jonkheijm@utwente.nl

J. Rouwkema
Department of Biomechanical Engineering, University of Twente, Drienerlolaan 5, 7522NB Enschede, The Netherlands

W.H. Nijhuis
Department of Orthopaedic Surgery, University Medical Centre Utrecht, Wilhelmina Children's Hospital, Lundlaan 6, 3548EA Utrecht, The Netherlands

A.D. van der Meer
Department of Bioengineering Technologies, University of Twente, Drienerlolaan 5, 7522NB Enschede, The Netherlands

Keywords: organ-on-a-chip, correlative light and electron microscopy, volume electron microscopy, live fluorescence microscopy, bone-on-a-chip

Abstract:
Organs-on-a-chip are of increasing interest for studying tissue development in health and disease. In the past years, platforms have been developed to analyze developmental biological processes by light microscopy and biochemical assays. While these show great potential for pharmaceutical applications, retrieving ultrastructural information about microtissues remains challenging. In this study, an organ-on-a-chip is presented that is suitable for analysis by correlative light and electron microscopy. Using osteogenic cultures in which the cells and deposited collagen matrix align between pillars, the applicability of this platform for high-resolution, longitudinal monitoring of the microtissue development during multiple weeks with 3D live fluorescence microscopy is shown. The analysis of complete microtissues showed the development of two distinct actin patterns during differentiation. Furthermore, intact microtissues were extracted and cryo-fixed by high-pressure freezing, to enable processing for volume electron microscopy. The region of interest for electron microscopy was selected based on the fluorescence images and the resulting FIB/SEM image stack shows ultrastructural information about the cellular organization, collagen alignment, and mineralization in the cultures. The platform developed in this study shows great potential for increasing our understanding of processes underlying structural organization of tissues in health and disease, by allowing ultrastructural analysis of tissues during development.

Table of Contents:

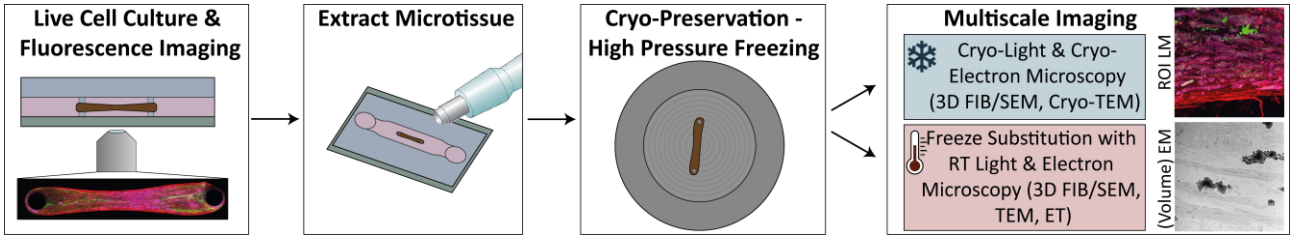

An organ-on-a-chip is presented that is suitable for high-resolution fluorescence microscopy over multiple weeks and from which intact samples can be extracted for analysis by volume electron microscopy. A case-study with osteogenically differentiated microtissues showed the development of two types of actin patterns during differentiation. Subsequent electron microscopy showed the presence of aligned cells and collagen, as well as mineral deposition.

Introduction

In recent years there has been an increasing focus on replacement, reduction, and refinement in animal research (the 3R principle).[1] Therefore, the interest in physiologically relevant cell culture models to study organ development is rising and much progress has been made in the development of (3D) organ-on-a-chip devices. Organs-on-chip combine microfluidics and tissue engineering to mimic a specific aspect of an organ[2] and allow for the precise control of nutrients and signaling factors in the culture, as well as the application of mechanical stimuli, to closely mimic a physiologically relevant dynamic microenvironment.[3] The highly reproducible organ-on-a-chip devices are regularly used to mimic tissue interfaces, such as the alveolar-capillary interface of the lung[4] and the intestine.[5] Moreover, on-chip cultures resembling complex 3D tissues have been developed, such as heart-on-a-chip devices in which mechanical stimulation promotes synchronous beating and improved contractile capability in response to electric pacing.[6] These devices provide great promise for studying the physiological and pathological processes during tissue morphogenesis and for the *in vitro* testing of therapeutic strategies.[3c]

Next to offering a wide range of custom-made organ-on-a-chip platforms for various organs,[2a] microfluidic culture platforms have also been standardized for commercialization in the past years by several companies, mainly focusing on pharmaceutical applications.[3a, 7] Due to the transparent materials used for most custom-made and commercial organ-on-a-chip devices,[3b] live monitoring of culture development in organ-on-a-chip devices using light microscopy is commonly applied in these systems.[7a] Furthermore, the enclosed, sterile environment of organ-on-a-chip devices allows for monitoring of development during multiple weeks to months, using live (fluorescence) microscopy.[2b] However, the spatial resolution of the imaging is limited by the accessibility of the sample for a microscope objective, which is often dependent on the chip design.[7a, 8] Higher resolution can be obtained using (volume) electron microscopy approaches. However, due to the relatively large size of these chips (millimeter-scale) the microtissue needs to be cut open and only small pieces of the original sample can be used for ultrastructural analysis by electron microscopy. This limits the possibility of combining live fluorescence imaging data with ultrastructural information in a controlled fashion, which could be valuable to elucidate developmental pathways in tissue development, such as structural organization or transport pathways.

In this study, we have developed an organ-on-a-chip device that can be used as an advanced 3D imaging platform. Our platform enables live fluorescence imaging of the entire developing microtissue without compromising on resolution to visualize local variations in the culture during development, which could be overlooked when regional imaging is performed. Furthermore, our device is suitable for correlative light and electron microscopy (CLEM) applications, which allows us to visualize the microtissue ultrastructure in a region of interest with nanometer detail. Additionally, the application of mechanical stimuli, such as fluid flow or compression, is possible to better resemble human physiological stimuli in the tissue.

As a case study for applying this microfluidic imaging platform, we used human mesenchymal stem cells (hMSCs) to develop a bone-on-a-chip culture in an osteogenic setting. In the past decades, various approaches to generate 3D cell cultures of bone have been published,[9] in which osteogenic cells are cultured in a 3D environment, supported by a scaffold or matrix. However, the development of advanced, physiologically relevant 3D models for bone, such as bone organoids and bone-on-a-chip devices that include nutrient control, mechanical stimuli, and a hierarchical matrix organization resembling the bone matrix organization, is lagging behind. This is most likely due to the complexity of the tissue,[10] in which cell differentiation and the production of a mineralized matrix occur simultaneously. Adding to this complexity are local differences in the tissue, where on separate locations different cell types are responsible at the same time for the formation (osteoblasts) and resorption (osteoclasts) of this mineralized matrix, and the critical influence of mechanical stimuli on bone formation, resorption and organization.[11]

In the past years, the first bone organoids[9b, 12] and bone-on-a-chip cultures[13] were reported. Each of these cultures focuses on resembling specific characteristics of the human bone, such as the woven bone stage[9b] or osteocyte development.[13b] Furthermore, the beneficial effect of mechanical stimulation on bone cell cultures was shown using 3D cultures in bioreactors[9b] or perfused microfluidic devices.[13d, 13e] Ideally, culture models to study bone biology and

bone development should replicate the cell-cell interactions as well as the physiological mechanical stimuli, the hierarchical organization of the cells, and the development of a mineralized matrix.

With the development of the bone organoid-on-a-chip presented in this study, we monitored the early phases of matrix formation during osteogenic matrix development (up to 42 days). Optimizing this device for compatibility with a (cryo-)correlative imaging workflow allowed us to analyze the ongoing processes live with fluorescence microscopy, after which ultrastructural information was obtained using electron microscopy. By including fluid flow as a mechanical stimulus, we set a first step towards designing a culture in which early bone matrix formation can be studied in a physiologically relevant environment. This system may be further extended by including multiple cell types and by applying compression to resemble the forces sensed during movement to better study the effect of strain in tissue development. Achieving such realistic 3D bone model systems on an advanced imaging platform, where mechanical and (bio)chemical signals can be applied in a dynamic environment, will provide an important tool to enhance the understanding of bone modeling.

Results

Development of an Organ-on-a-Chip Platform for Multiscale Imaging

To visualize tissue developmental processes, such as early bone matrix formation, in high resolution over long-term periods, we set out to develop an organ-on-a-chip platform suitable for culturing 3D microtissues, based on a polymeric substrate (polydimethylsiloxane, PDMS) and precision cover glasses, that can be used in our multiscale imaging workflow **(Figure 1)**. To enable culture fixation and the possibility to influence the structural organization of the microtissue, PDMS pillars were introduced in the culture chambers in variable numbers, and the shape of the culture chamber was varied (Figure 1A).[9a, 9c, 14] The design of the chips was optimized for electron microscopy after cryo-fixation through high-pressure freezing (HPF). HPF allows physical fixation of the tissue and replaces conventional chemical fixation to minimize fixation artifacts.[15] Based on the requirements for HPF, the dimensions of the culture chamber in the chip were determined (Figure 1B). Since optimal preservation by HPF can be reached for samples up to 200 µm thick,[16] the total height of our culture could not exceed this number. However, as we expected the cell culture to contract after seeding because of cellular contraction, and to allow the inflow of a viscous suspension of cells in a supporting matrix, the chamber height was set at 400 µm, which indeed resulted in a 3D culture of approximately 100 µm thick. Furthermore, the carriers that we used for HPF have an inner diameter of 2 mm, which defines the limit for the length of the culture (Figure 1D). To ensure that the developing microtissues would fit this dimension, the 100 µm wide PDMS pillars that stabilize the culture were placed at a distance of 1.1 mm and the width of the culture chamber was set between 1 mm and 2 mm, dependent on which design was used.

To mimic physiological environments as closely as possible, the design of our organ-on-a-chip platform included possibilities to apply a continuous fluid flow resembling blood flow (Figure 1C, Supplementary Figure 1A), however, the device can also be used in static conditions. This allowed for the optimization of experimental conditions to experiment-specific requirements and offered the opportunity to test deferent regimes of mechanical stimulation.

The suitability of our platform for cryo-fixation (HPF) and application in multiscale imaging were based on the possibility of punching the complete microtissue out of the PDMS chamber using a standard skin biopsy punch with a diameter of 3 mm to ensure a perimeter of the punched area around the microtissue, and subsequently releasing the sample from the pillars (Figure 1D). After extracting the microtissue from the chip, the cell culture was released from the PDMS pillars with a needle to transfer the sample to cryo-preservation carriers for HPF. During this process, the shape of the microtissue remained intact, allowing for visual confirmation of the orientation based on the holes in the tissue on the site where the tissue had been surrounding the pillars. After HPF, the sample could be used in a workflow applying cryo-light and cryo-electron microscopy in 3D or the sample could be prepared for imaging at room temperature with freeze-substitution to replace the vitrified ice by a resin.[15]

To reduce complexity and demonstrate the working principle of this imaging platform, we mainly focused in this study on the application of advanced live imaging and subsequent volume electron microscopy in a static culture system. However, we have enabled the application of fluid flow on microtissues using an Ibidi® perfusion system (Supplementary Figure 1A). We here used osteogenic cultures as a case study for longitudinal live fluorescence imaging because of their long differentiation period extending over multiple weeks.[17]

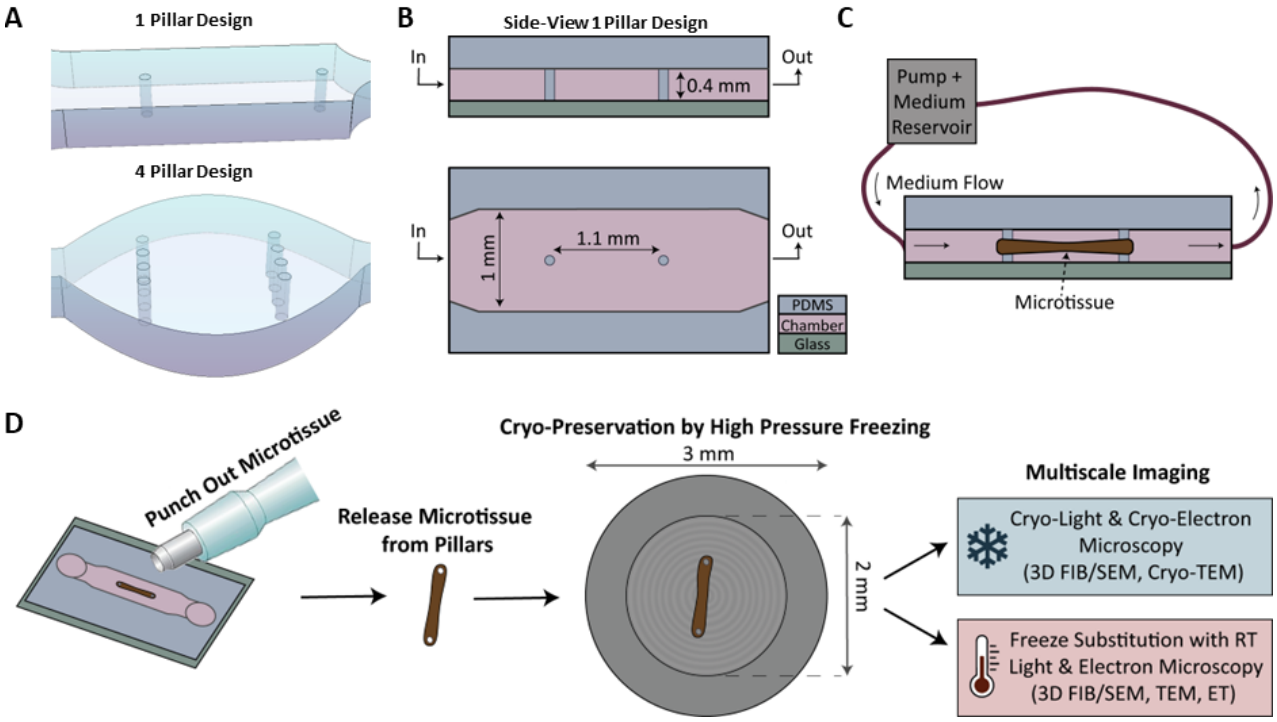

Figure 1 - Design of an organ-on-a-chip platform for multiscale imaging
A) 3D representation of two chip designs to influence the structural organization of 3D cell cultures in the chip. PDMS pillars are present in variable orientations to fix the cell culture and modify the culture organization. Designs with microfluidic burst valves were based on Cofiño-Fabres et al.[14e], however, in our design the PDMS pillars reached the full height of the chamber to fix the position of the pillars.. B) Schematic side- and top-view of an organ-on-a-chip platform for fixed and aligned cell cultures. PDMS chips are closed with cover glasses, permitting the use of live fluorescence microscopy. The channel width of the cell culture chamber is 1 mm in the linear channels and 2 mm in the round channels. The height of the culture chamber is 0.4 mm. PDMS pillars of 0.1 mm in diameter are placed at a distance of 1.1 mm to support and fix 3D cell cultures. C) Schematic representation of the application of a continuous medium flow through the in- and outlet of the organ-on-a-chip in which a microtissue is growing between two pillars. D) Schematic overview of pipeline to transfer samples from our organ-on-a-chip platform to light- and electron microscopy: whole samples are punched out of the PDMS chips using a biopsy punch and are released from the pillars. Isolated microtissues are transferred to high-pressure freezing carriers (gray circle) for cryo-preservation by HPF. After cryo-preservation, samples can be used for multiscale imaging by either cryo-light and cryo-electron microscopy or freeze-substitution with subsequent room-temperature light and electron microscopy.

Longitudinal Monitoring of the Bone Microtissue Development

To visualize the early stages of bone matrix development during osteogenic differentiation, human mesenchymal stem cells (hMSCs) were loaded on chips with various pillar configurations as a suspension in fibrin gels, which initially supported the 3D culture. The cells were cultured in an established osteogenic medium, to induce cellular differentiation and matrix formation.[18] Shortly after seeding, upon stretching and adhesion, the cells contracted the gel around the pillars, yielding microtissues of different shapes (**Figure 2**A-B). Visualization of the complete cultures in 3D (Figure 2A-B, Supplementary Figure 2A) showed the dependence of the culture structure on the number and location of the pillars. After seven days of differentiation, maximum intensity projections showed that not only the organization of the cells (red, actin), but also the organization of the deposited collagen (green) had adjusted to the pillar-induced strains (Figure 2A, Supplementary Figure 2B). In each of these bone-on-a-chip devices, the cultures could be differentiated and fluorescently imaged for multiple weeks, which allowed us also to visualize the mineralization of the developing matrix (magenta, Figure 2B, Supplementary Figure 2C), a crucial step during bone formation. Interestingly, differences in the intensity of the mineral signal were observed between different locations in the cultures, with a generally increased mineralization at the curved regions of the microtissue that surrounded the PDMS pillars (Figure 2B). Since collagen alignment is a main characteristic of the bone matrix and defines the mechanical properties of bone, we decided to continue to work with the devices in which two single pillars were fixing the cultures (1 pillar design, one pillar on either side of the chip), as these showed the most unidirectional collagen organization.

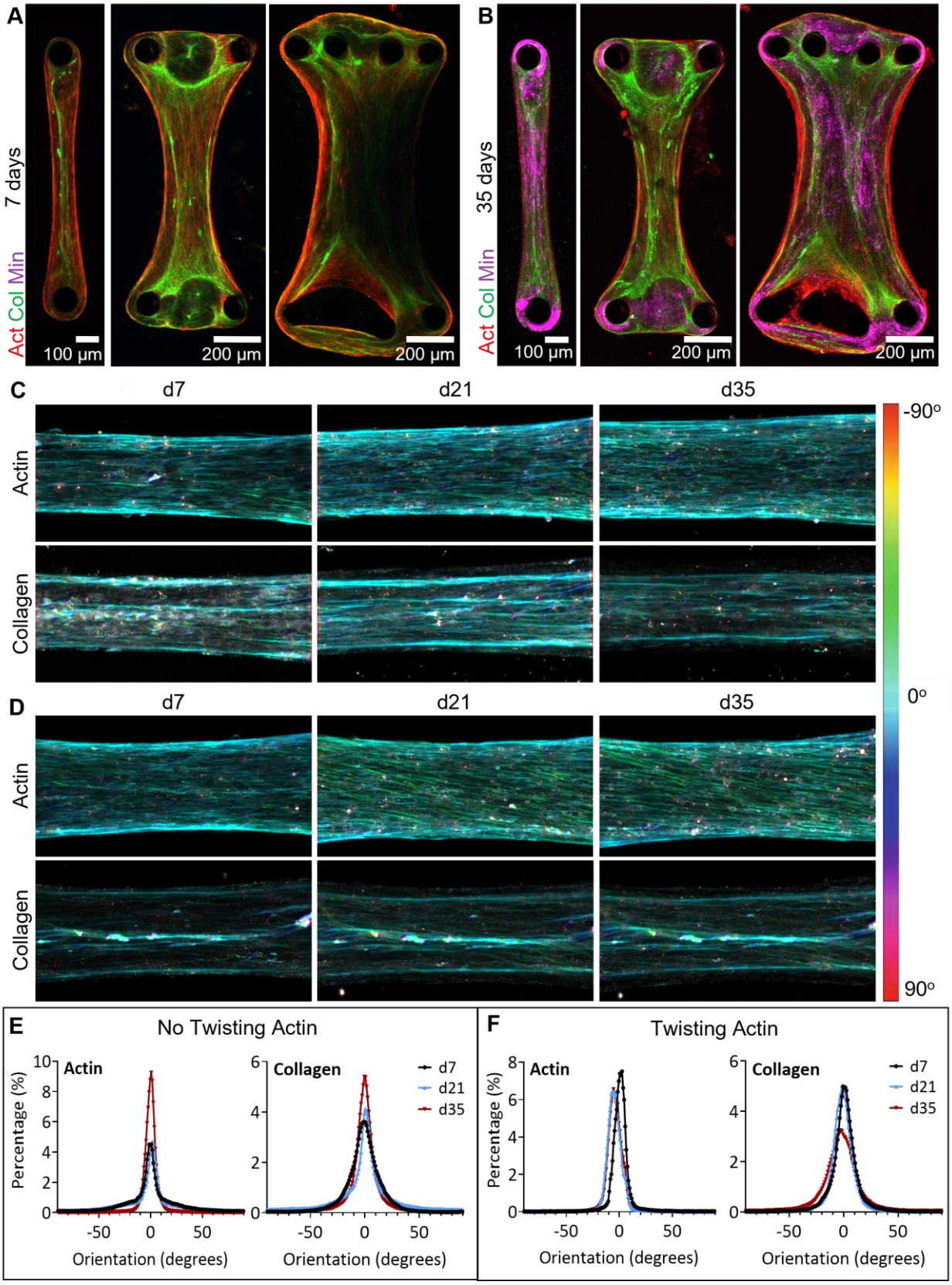

Figure 2 - Live monitoring of the development of a bone-on-a-chip culture

A/B) hMSCs were seeded in fibrin gels and differentiated along the osteogenic lineage to grow bone-on-a-chip cultures. Cultures in chips with multiple pillar arrays (1/2/4 pillars per side of the chip) were visualized using fluorescence microscopy after 7 and 35 days of differentiation under static conditions. Maximum intensity projections showed aligned actin (SiR-actin, red) and collagen (CNA35-OG®488, green) patterns after 7 days of differentiation (A). Mineral (Calcein

Blue, magenta) was observed mainly in the bent tissue around the PDMS pillars after 35 days of differentiation (B). Corresponding orthogonal views are shown in Supplementary Figure 2A. C-D) Color-based orientation analysis on maximum intensity projections of differentiating cultures (in chips with 1 pillar on each side) showed two types of patterns of actin organization during differentiation: actin orientation remained stable and parallel to the strain direction (C) or started twisting (D) during differentiation. Collagen orientation remained stable over time in both situations. E/F) Orientation histograms showing the preferred orientation confirmed the observation of static (E) or twisting (F) actin during differentiation with a stable collagen orientation.

As the complete microtissues could be imaged live during osteogenic differentiation, weekly monitoring of actin and collagen patterns in the cultures made it possible to study the organizational development of the culture. A color-based orientation analysis of the fluorescence images showed that the cellular actin pattern of the cultures could have two different types of morphologies, which stretched throughout the full culture (Figure 2C-D). The actin signal was either observed in a straight pattern, which approximately aligned to the strain direction between the pillars (Figure 2C), or in a diagonal pattern, in which the actin did not align with the direction of the strain and the cells formed a twisted turn around the culture (Figure 2D, d21/d35). Interestingly, in samples showing the diagonal pattern, the global actin orientation changed during differentiation, while the collagen orientation, parallel to the strain direction, remained stable over time (Figure 2D). This was also visible in the plotted orientation distributions of the samples (Figure 2E-F), which showed that the preferred orientation of the actin was stable in samples that did not show an actin twist (Figure 2E), while it was changing in samples that showed the twisting actin (Figure 2F). In contrast, the preferred orientation of the collagen remained stable during differentiation in both sample types. Based on the imaging of the complete culture over long time scales, we conclude that the observed differences were not dependent on the location of imaging, but the patterns were characteristic for the complete microtissue.

Characterization of the Developing Bone-on-a-Chip in 3D

To better monitor the developmental processes in the cell culture, such as collagen production and mineralization, we analyzed our bone-on-a-chip cultures with advanced live imaging, using Airyscan® fluorescence and Raman microscopy (**Figure 3**). We first recorded fluorescent z-stack images of the complete culture during osteogenic differentiation, to determine a region of interest (Figure 3A, 28 days differentiated). The orthogonal views (Figure 3A_i-A_{ii}) showed that the cultures have a symmetrical shape in the central region, with the most dense actin signal located in the periphery of the culture surrounding a layer of collagen. In the inner core of the culture, cells were also present, even though the density of cells in this region was lower than in the peripheral layer that is in direct contact with the culture medium. Next, we zoomed in to visualize a defined region of interest with high resolution (voxel size: 41 x 41 x 160 nm) using a water immersion objective to minimize refractive index mismatching caused by the various interfaces (glass/medium/culture) that are crossed during imaging (Figure 3B). The maximum intensity projection (Figure 3B, XY) showed the alignment of actin (red) and collagen (green), while the orthogonal views (Figure 3B_i-B_{ii}) showed the organization of the cells and collagen throughout the depth of the culture. The fixation of the culture by the pillars allowed us to identify the orientation of the culture in a reliable fashion, which is essential for this zoom-in approach and the subsequent correlative electron microscopy.

To characterize the chemical composition of the early mineralizing culture in more detail, Raman spectroscopy mapping was performed on cultures after three weeks of osteogenic differentiation in the presence of fluid flow (0.8 ml/min). These cultures showed similar collagen and mineralization patterns as static cultures, but mineralization was observed earlier during differentiation (day 21, Supplementary Figure 3A). Raman depth scans were recorded in two regions, one close to the pillar where the mineral signal was highest in fluorescence microscopy (Figure 3C-E) and one in the center of the culture in which cells and collagen usually showed an aligned morphology (Supplementary Figure 3B-D). True component analysis was used to identify three spectral components in the region close to the pillar, comprising the mineralized matrix (component 1, green), carbonated hydroxyapatite (component 2, magenta), and cellular material with mineral (component 3, blue, Figure 3D-E). The mineralized matrix (component 1) was identified by the presence of the v1 PO_4^{3-} vibration at 960 cm^{-1},[19] together with organic vibrations (amide III (~1250 cm^{-1}), CH_2 (~1450 cm^{-1}))[19] and the depth scan showed that this was mainly present near the core of the culture (Figure 3D-E, green). From the relative peak heights of the phosphate and organic vibrations, it became apparent that the matrix in this region of the culture was hyper-mineralized. Component 2 also showed the presence of a clear v1 PO_4^{3-} vibration at 960 cm^{-1}, as well as a v2 CO_3^{2-} at 1072 cm^{-1},[19] from which we concluded the presence of carbonated hydroxyapatite. From the depth scan it became apparent that this carbonated hydroxyapatite was localized in a round spot, and based on the presence

of these two peaks, and the low number of other identified vibrations, we concluded that this was a spot of precipitated mineral (Figure 3D-E, magenta). The top layer of the depth scan (blue, component 3) contained a number of organic peaks (amide III (~1250 cm^{-1}), CH_2 (~1450 cm^{-1}))[19] as well as a small mineral peak (960 cm^{-1}), which indicated the presence of both cells and mineral in this region. Overall, the distribution of cells and matrix was similar to the distribution observed in fluorescence microscopy. In contrast to the region close to the pillar, the Raman spectra of the region in the center of the culture (Supplementary Figure 3D) showed very low mineral-related signals, while the peaks representing cellular material (blue, component 1) and organic matrix (green, component 2) were more pronounced, which was based on the peak around 1340 cm^{-1} were more pronounced.[19] These components were localized similar to the previously observed distribution (Supplementary Figure 3C) in which the cells surrounded a collagen layer.

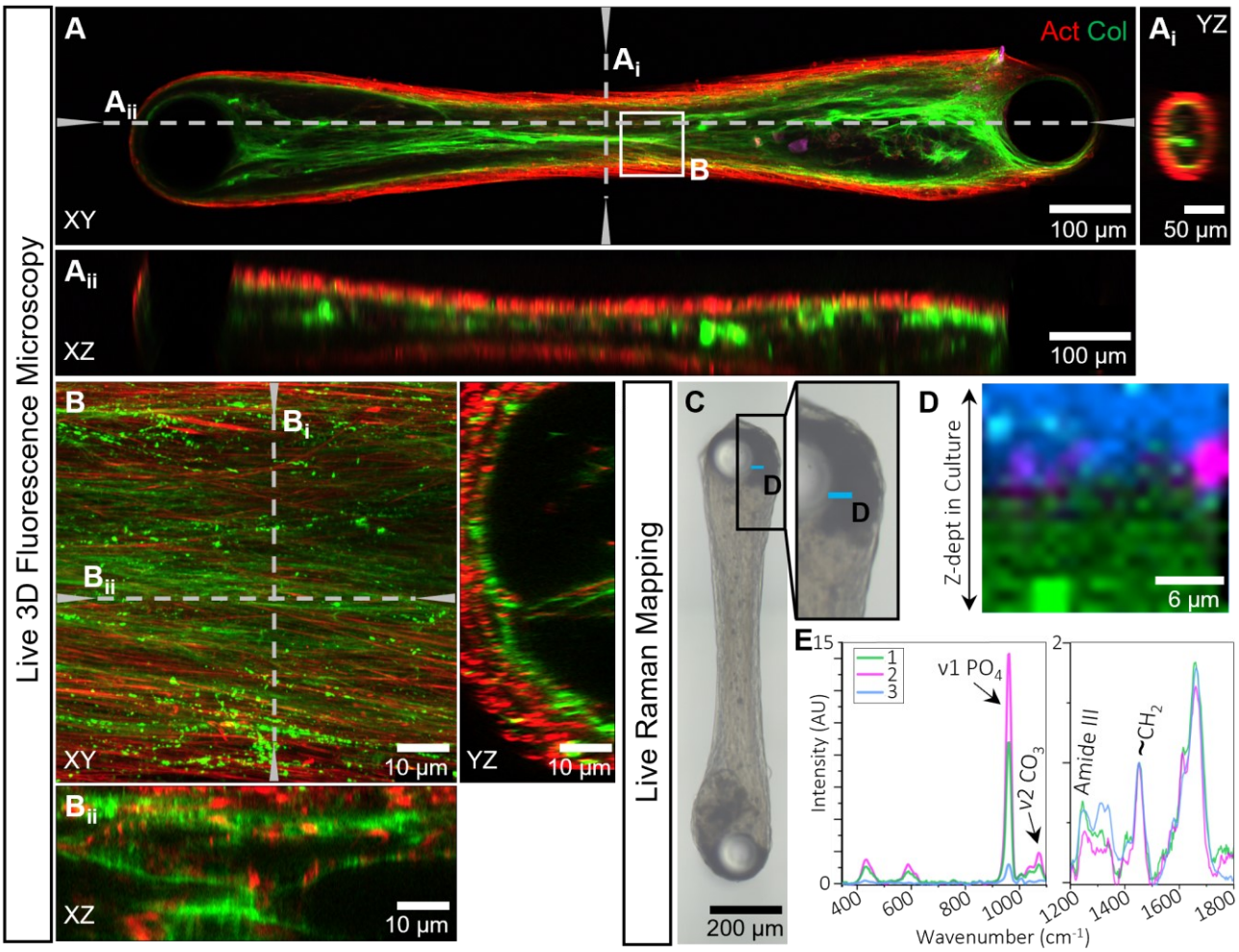

Figure 3 – Advanced live imaging of an aligned bone-on-a-chip culture

A-B) Live 3D fluorescence microscopy on-a-chip. A) Live fluorescence microscopy of a complete bone-on-a-chip culture after 28 days of differentiation (A) showed actin (SiR-actin, red) and collagen (CNA-OG®488, green) distributions in 3D. Orthogonal views (A_i: YZ, A_{ii}: XZ) revealed the cylindrical structure of the culture between the two pillars. Orthogonal views were made at the locations indicated by the dotted lines (A_i and A_{ii}). Images were recorded with a 10x objective (NA 0.4, voxel size: 124 x 124 x 1420 nm). B) High-resolution imaging (63x, NA 1.2, voxel size: 41 x 41 x 160 nm) of a region of interest in the center of the culture in 3D showed detailed information regarding the collagen and cellular organization in the culture. Collagen (green) was observed as assembled fibrillar structures (lines) and, presumably, newly secreted matrix (dots). Orthogonal views from the locations indicated by the dotted lines. C-E). Live Raman spectroscopy mapping on-a-chip. C) Optical image of a living bone-on-a-chip culture exposed to fluid flow (0.8 ml/min) taken by a Raman microscope after 21 days of differentiation. The region of interest around the pillar in which Raman depth mapping was performed is indicated (blue line, D). D) Spatial distribution of TCA components identified in Raman depth map localized near the PDMS pillar in the bone-on-a-chip culture. E) Spectra which match with the components in D identified 1) mineralized matrix (green), 2) carbonated mineral precipitation (magenta) and 3) cellular components with a low amount of mineral (blue).

260 ***Correlative Light and Electron Microscopy of a Mineralized Bone-on-a-Chip Culture***

261 After establishing the zoom-in approach to identify and localize a region of interest at multiple magnifications in live
262 imaging, we set up a CLEM experiment to visualize the cell-matrix interactions and assess the mineral deposition during
263 early osteogenic matrix formation in more detail (**Figure 4**). We monitored the culture development using live
264 fluorescence microscopy by weekly staining the actin, collagen, and mineral in the culture (Supplementary Figure 4A).
265 After 35 days of differentiation, the first mineral signal was observed and the microtissues were kept in culture for one
266 more week to allow the further development of the mineralization. At day 42 of differentiation (Figure 4A), we extracted
267 the microtissue and cryo-fixed the differentiated osteogenic cultures within minutes after live fluorescence microscopy
268 by HPF using the previously described punching method (Figure 1D) and prepared the samples for electron microscopy.
269 To confirm the localization of the sample in the carrier, before HPF an overview fluorescence image of the extracted
270 microtissue was made in low resolution (Figure 4B). After HPF, the cryo-preserved sample was visualized again using
271 cryogenic fluorescence microscopy (Figure 4C) to confirm the successful processing of the sample before automated
272 freeze substitution was started to embed the sample in a resin. After resin embedding, part of the microtissue in the
273 block was imaged using room temperature fluorescence microscopy to record overviews (Figure 4D) and z-stacks of
274 regions of interest (Figure 4D_i-D_{ii}).

275 Based on the cellular alignment and mineral signal, region D_{ii} (Figure 4D) was selected as our target region for volume
276 electron microscopy. To allow for identification of this region in electron microscopy, the reflection image of the freeze
277 substituted sample was recorded in parallel to the fluorescence imaging of the resin embedded sample (Figure 4E). This
278 reflection image showed the presence of a ring structure with scratch marks (Figure 4E, blue marks 1, 2 and 3), which
279 were imprinted in the resin by the HPF carrier and the remaining shape of the pillar (Figure 4E, blue mark 4). Next, a
280 top-view image of the sample was recorded with SEM (Figure 4F), where the same ring structures, scratches, and pillar
281 shape were identified (Figure 4F, blue marks). Using Zeiss Zen 3.7 software with Zen Connect, the two images could
282 then be overlayed, and the overlay was used to identify the region for 3D focused ion beam scanning electron
283 microscopy (FIB/SEM, Figure 4G, blue line). By overlaying the SEM top-view of the sample after 3D FIB/SEM with the
284 previously recorded top-views in light and electron microscopy, the exact imaged volume could be targeted in the
285 fluorescence z-stack (Figure 4H). As expected based on the fluorescence microscopy, the FIB/SEM images showed the
286 presence of aligned cells, as well as fibrillar structures, which we identified as collagen (Figure 4I, Supplementary Figure
287 4B). The presence of aligned cells was observed through the complete stack, and cellular organelles could be recognized
288 (marks in Supplementary Figure 4B). While proceeding the imaging towards the center of the culture (deeper in the
289 stack), a denser layer of collagen appeared in the bottom region of the field of view (Figure 4I, left corner). Additionally,
290 electron-dense structures were observed between the cells, which we identified as mineral precipitations that were
291 present throughout the complete imaged volume (Figure 4I, Supplementary Figure 4B).

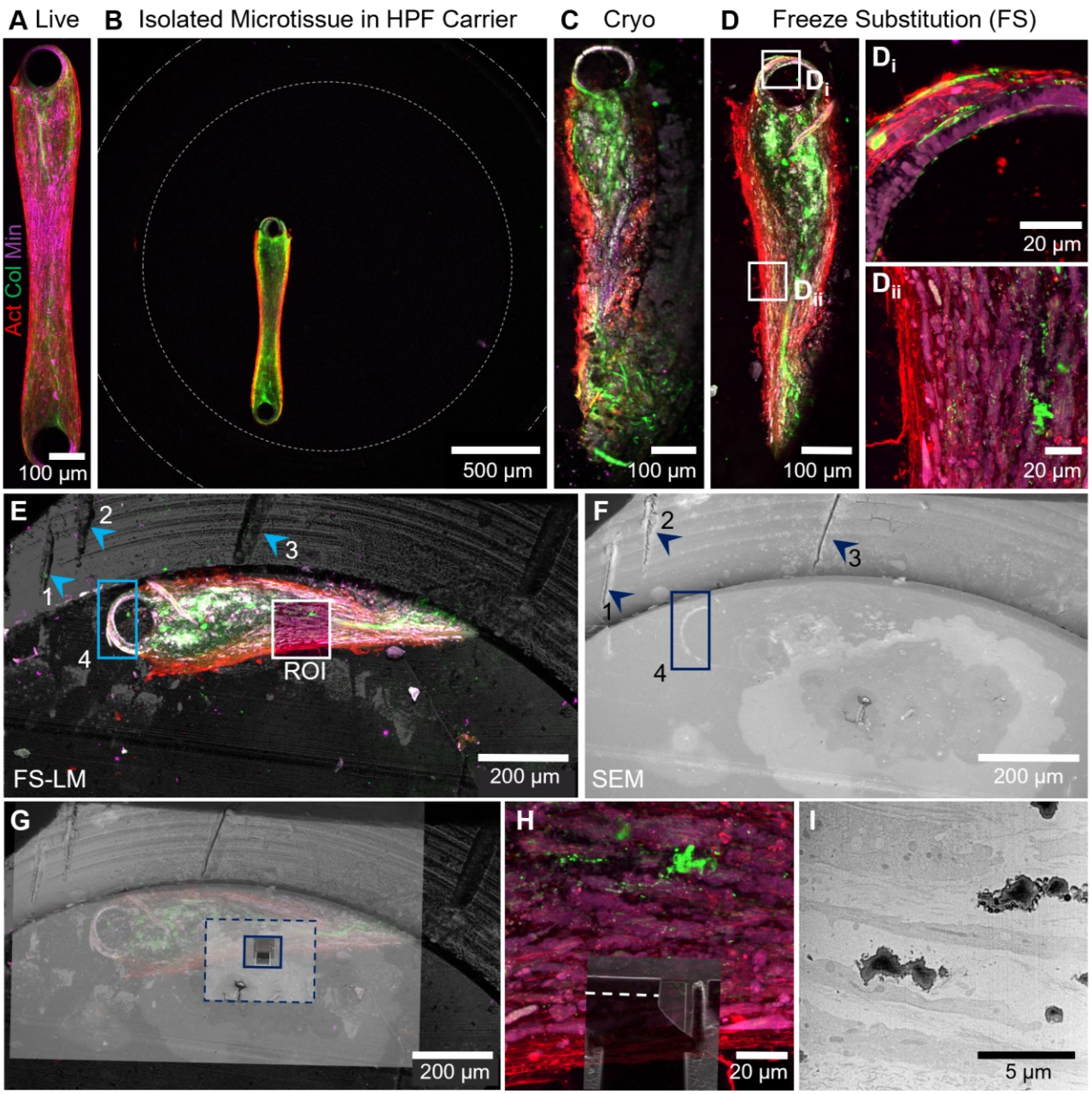

Figure 4 - Targeting a bone-on-a-chip culture for multiscale imaging in a defined region of interest

A) Live fluorescence microscopy of mineralized bone-on-a-chip culture (actin: SiR-actin, red; collagen: CNA35-OG®488, green; mineral: Calcein Blue, magenta; maximum intensity projection) after 42 days of differentiation. B) Overview image of isolated microtissue after transfer to cryo-fixation carrier for HPF. Dotted lines indicate the inner and outer diameter of the carrier. Image was recorded with a 5x objective (NA 0.2). C) Cryo-fluorescence microscopy showed the successful transfer and cryo-preservation of the microtissue (maximum intensity projection). D) Overview of the maximum intensity projection of room temperature fluorescence microscopy after automated freeze substitution (FS) in Lowicryl HM20 resin and determination of regions of interest for high-resolution z-stacks (D_i/D_{ii}). Maximum intensity projections of high-resolution stacks (40x water immersion objective, NA 1.0, voxel size 49 x 49 x 260 nm) around the pillar (D_i) and in the center of the culture (D_{ii}). E) Overlay of fluorescence and reflection microscopy of a resin embedded bone-on-a-chip after freeze substitution for correlation with SEM. Marks for correlation are indicated in blue. F) Top-view of the resin embedded sample in SEM (XY in light microscopy) of the same region as visualized with light microscopy in E, for correlation and identification of location of region of interest. Marks for correlation are indicated in blue. G) Overlay of top-view of light and electron microscopy, showing step-wise alignment (dotted blue line) to determine location of the trench for FIB/SEM (solid blue line). H) Overlay of maximum intensity projection of high-resolution fluorescence microscopy of region of interest (D_{ii}) overlayed with top-view of trench after FIB/SEM volume imaging has

been performed. The location of the FIB/SEM image represented in I is indicated with a dotted line. I) Front-view SEM image from FIB/SEM stack (XZ in light microscopy) in region of interest after 21 µm of milling and imaging.

Discussion

In this study, we have developed an organ-on-a-chip platform that is suitable for multi-scale imaging by optimizing our culture chamber to a minimized confined space in which a small 3D microtissue (around 100 x 100 x 1100 µm) could be grown. These dimensions allow for live fluorescence microscopy during tissue development, as well as cryo-fixation of the microtissue by HPF and subsequent targeted analysis of a region of interest by volume electron microscopy. The cryo-fixation is an end-point preservation technique, however, analysis of intermediate stages of the development process by conventional techniques that allow for live read-outs, such as biochemical characterization of the medium outflow would still be possible, which maximizes the potential output of these devices.

We used this platform to visualize the early phases of osteogenic differentiation, including matrix formation and mineralization. The pillar fixation of our osteogenic cultures allowed for cellular alignment upon contraction of the supportive fibrin matrix, comparable to what was shown previously for other cell types.[14c, 14d, 20] Additionally, this fixation induced alignment of the cell-produced collagen matrix, similar to what was shown in larger cell culture models,[9a, 9c, 14a, 14b] and allowed us to influence the culture organization by adjusting the pillar arrangements (Figure 2, Supplementary Figure 2). This flexibility increases the potential of our organ-on-a-chip platform to study not only osteogenic development but also other tissues with specific needs regarding the orientation of the tissue. Additionally, the mechanical stimulation of microtissues in the chip could be further expanded to enhance the physiological relevance of this model system. Initial experimental data together with computational modeling showed that compression on the chambers of the chips presented in this study is possible at various strengths, using a magnetic compression device (Supplementary Figure 1B-D). However, further optimization of the compression device is needed to improve the control over the magnetic actuation and enable compression of microtissues in a static as well as dynamic fashion.

We showed that it is essential to image the complete, living microtissue without compromising on the spatial imaging resolution to identify local differences in the osteogenic tissue during differentiation and to study sample-specific patterns during the microtissue development. The local differences in mineralization between curved tissue around the PDMS pillars and the center of the culture (Figure 2) may be explained by local strain differences in the microtissues, which have been identified in previous studies,[14c, 20] and would confirm the reported beneficial influence of strain on osteogenic differentiation.[21] However, additional confirmation of the differentiation status of the cells in different locations of the culture is needed, for example by antibody stainings for osteoblast markers.

The longitudinal imaging of the complete microtissue also enabled us to identify two distinct actin patterns that developed during differentiation (Figure 2). Since we imaged the complete microtissues and targeted the same region for analysis at each timepoint, we could exclude that the observed differences were caused by imaging at multiple locations in the sample. Furthermore, the live imaging strategy allowed us to exclude sample-to-sample variations, which may be introduced by imaging different samples at multiple timepoints during development as is commonly done in embryonic animal studies.[22] The observed diagonal actin patterns proceeded throughout the complete culture and developed over time, similar to what was previously shown for monolayer mouse osteoblast cultures seeded on curved substrates.[23] Previous studies also showed that surface curvature was underlying the development of twisted actin patterns by osteoblasts.[23-24] However, since our cultures all started as comparable, rectangular shapes based on the chamber design and self-organized into tissue straps, no difference in the growth conditions, like surface curvature, was expected. Therefore we hypothesize that other factors, such as sample-specific mechanical stiffness due to differences in collagen production speed and fibrin degradation rate, may influence the development of these actin patterns in our 3D culture system. This shows the potential of our organ-on-a-chip platform to study mechanistic processes in tissue development. However, the exact mechanisms and dynamics involved in the development of the two identified actin patterns remain to be elucidated.

Using our bone-on-a-chip as a case study, we showed the potential of fluorescence microscopy on HPF fixed, resin embedded samples to guide the volume electron microscopy to our region of interest. While analyzing cellular organization in organoids by volume electron microscopy and correlative microscopy is a valuable tool to study organ development and disease conditions,[9b, 25] a similar analysis of 3D microtissues, grown in microfluidic platforms has not been previously reported. The organ-on-a-chip platform presented in this study thereby opens the possibility to extend

the analysis of microphysiological devices with targeted ultrastructural analysis in 3D. Further improvements could be made to allow optimal correlation of the fluorescence and electron microscopy volumes by controlling the orientation of the microtissue in the cryo-fixation carriers, as was achieved by direct culturing of organoids in cryo-preservation carriers.[25a] Moreover, the addition of fiducial markers and internal small organelle labeling for the correlation of multiscale data could enhance the quality of the correlation.[26]

Next to osteogenic cultures, our organ-on-a-chip platform could be used to study the development of other tissues that show millimeter scale organization, such as muscle,[14c, 27] tendon[27] or cornea,[28] as the chip design could be optimized to stimulate the formation of variable tissue organizations by adjusting the pillar arrangement.[14d] Furthermore, the complexity of the microtissues could be increased by including additional cell types, such as osteoclasts in the bone-on-a-chip culture or endothelial cells for the vascularization of microtissues. Initial studies have already shown the potential of organ-on-a-chip devices for co-culture models.[7a, 13d] However, the combination with high-resolution imaging as shown with our platform could further enhance the understanding of the tissue development by providing detailed information on the cell-cell interactions in these co-cultures. Furthermore, the application of mechanical compression on the cell culture could improve the physiological relevance of our platform by mimicking the forces sensed by tissues during daily activity.[7a, 29] Preliminary experiments showed the functionality of a custom-made holder including pins and magnets to apply compression on our microtissues (Supplementary Figure 1B). However the design needs to be optimized allow for dynamic compression regimes to resemble cyclic compression, as sensed for instance by bones during human movement.

Conclusion

In this research, we showed the development of an organ-on-a-chip platform that enables the detailed and dynamic analysis of the developing microtissues with correlative imaging in cryogenic or room temperature conditions. This platform allows for live monitoring of the complete tissue during multiple weeks of development and the ultrastructural analysis of the sample at a moment and region of interest. Furthermore, adaptation of the device to tissue-specific requirements is possible, by modulation of the pillar configurations and inclusion of mechanical cues like fluid flow and compression. As only the cryo-fixation step is destructive for our device, this platform is also suitable to be used in combination with conventional biochemical analysis of the culture medium to monitor secreted factors during tissue development. We therefore expect that the application of this platform will further improve the current understanding of processes involved in tissue development and structural organization in health and disease, which could help to identify new therapeutic targets for a wide range of diseases, including bone-related diseases, such as osteogenesis imperfecta. Additionally, these platforms are expected to aid in the development of strategies for personalized medicine, by developing patient-specific cultures to test drug efficacy in an individualized, physiologically relevant setting.

Materials & Methods

Materials

Chemicals and cell culture supplements were purchased from Sigma-Aldrich/Merck unless indicated differently. Cell culture media and antibiotics were from Gibco.

Chip production

A mold for chip production was milled from a 5.5 mm thick, cast Altuglas® poly-methyl methacrylate (PMMA) sheet (Arkema) using a micromill (Datron Neo). After producing the mold, it was cleaned by rinsing with MilliQ, followed by absolute EtOH rinsing and blow drying under a flow of N_2. Next, dimethylsiloxane monomer of a Dow Sylgard 184 elastomer kit was mixed with the curing agent (ratio 10:1) and carefully degassed *in vacuo* to remove air bubbles. Then, the mold was surrounded with sticky tape to provide a removable barrier and the degassed mixture was poured onto the mold. The covered mold was then degassed *in vacuo* to remove air bubbles and to allow the mixture to completely fill all features of the mold. The degassed mixture on the mold was cured at 80°C for 1 h. Afterwards, the polydimethylsiloxane (PDMS) was carefully peeled off and the unbonded PDMS chips were separated by cutting with a 18 mm wide scraper (Tajima) equipped with a Razar Black Blade®.

405 Next, 10:1 monomer:curing agent of the Sylgard 184 kit was diluted in heptane (200x). Glass coverslips (#1.5, Thorlabs)
406 were spin coated with the resulting solution (6000 rpm, 30 s, 2000 rpm/s acceleration) and cured at 80°C for 30 min.
407 Using a disposable 1 mm diameter biopsy punch (KAI Medical, B49101), inlets and outlets were punched into the PDMS
408 chips. The unbonded PDMS chips and spin coated coverslips were exposed to oxygen plasma in a Diener Zepto Plasma
409 Cleaner (0.4 mbar, 90 W, 40 s) before bonding and directly after plasma treatment, the PDMS chips were bonded to the
410 coverslips, followed by a short post-curing step (5 min, 70°C) on a heating plate to improve adhesion.

411 Cell culture

412 Human mesenchymal stem cells (hMSCs, passage 2-6) isolated from a healthy female (11 years old) were kindly provided
413 by the department of Orthopaedics of the University Medical Center Utrecht (UMCU). For hMSC isolation, human bone
414 plus marrow waste material was obtained in accordance with the Declaration of Helsinki, with the approval of the
415 Assessment Committee Biobank (TCBio) of the University Medical Center Utrecht (Utrecht, The Netherlands) under the
416 approved number TCBio-18-685, and with the written consent of the parents. Isolated hMSCs were expanded in
417 proliferation medium (PM; αMEM (12571), 10% FCS (F7524), 100 U/mL-100 µg/mL Penicillin/Streptomycin (15140122),
418 0.28 mM L-ascorbic acid-2-phosphate (AA2P (49752)), 1 ng/mL recombinant human FGF (R&D Systems, 233-GMP-025))
419 in a humidified incubator (37°C, 5% CO_2). Upon 80% confluency, cells were split (1:10) by trypsinization (0.05%
420 Trypsin/0.53mM EDTA in PBS) according to standard cell culture protocols.

421 Chip seeding and maintenance

422 Bonded PDMS chips, were coated with Pluronic F-127 (1% in MilliQ, 20 min, RT (P2443)). After coating, the solution was
423 removed and the chips were connected to a vacuum suction system to dry the inside of the channels and culture
424 chambers. Fibrinogen (F8630, 60 mg/mL in αMEM supplemented with 2 mg/mL aminocaproic acid (ACA (A7824)); based
425 on 77% clottable protein) was diluted in complete PM, supplemented with ACA (2 mg/mL) to a final concentration of
426 6 mg/mL. Thrombin (605157, 50U/mL in αMEM) was diluted in complete PM to a final concentration of 5 U/mL.

427 hMSCs (passage 3-6) were trypsinized and resuspended in the thrombin solution ($2x10^6$ cells/mL). To induce gel
428 formation, the cell/thrombin suspension was mixed with the fibrinogen solution (volume ratio 1:1). Directly after mixing,
429 the chambers of the chips were loaded from one of the inlets. Afterwards, the solution was removed from the channels,
430 and cell suspension only remained in the chambers. The seeded chips (final concentration $1x10^6$ cells/mL) were placed
431 in the incubator (37°C, 5% CO_2) for 1 h before PM supplemented with ACA (1 mg/mL) was added to the channels, using
432 filter pipette tips as a medium reservoir.

433 After culturing the chips for two days in PM, the PM was replaced by osteogenic induction medium (OIM, PM
434 supplemented with 6 mM β-Glycerophosphate (βGP, G9422) and 100 nM dexamethasone (D4902)), supplemented with
435 ACA (1 mg/mL). Medium was refreshed 3 times a week during differentiation. To allow degradation of the fibrin scaffold,
436 ACA was left out of the OIM after 14 days of differentiation.

437 To apply fluid flow, we used an Ibidi® pump system. At the start of the differentiation (day 0), two diagonal inlets of the
438 chip were blocked using sterilized, blunt end needles (19G) filled with cured PDMS. The remaining two inlets were
439 connected via blunt end needles to the Ibidi® Luer connectors of an Ibidi perfusion set (red, 1.6 mm), that were
440 connected to the Ibidi® Fluidic Unit as described by the manufacturer, including pre-run equilibration to remove air
441 bubbles. The syringes connected to the perfusion set each contained 6 mL of OIM (supplemented with ACA (1 mg/mL)
442 during the first 14 days) and the total medium was changed once a week. Flow settings were calibrated to be 0.8 mL/min
443 and with valve switching times of 120 s.

444 Live fluorescence imaging of differentiating bone-on-a-chip cultures

445 Differentiating microtissues were stained live with silicon-rhodamine F-Actin (SiR-Actin, 1 µM + 10 µM Verapamil,
446 Spirochrome, SC001), CNA35-Oregon Green® 488[30] (CNA35-OG®488, 0.167 µM TU/Eindhoven, collagen staining) and
447 Calcein Blue (M1255, 0.1 mg/mL, mineral staining). All stainings were diluted in the same medium as the cultures were
448 grown in at that moment. Cells were incubated with the staining solutions for 2 h at 37°C. After staining, the cultures
449 were washed 3x with PBS, and fresh medium was added to the chips. Next, the inlets were closed with a coverglass and
450 the chips were placed upside-down on a object glass. Live cell imaging was performed on a LSM900 upright microscope
451 (Carl Zeiss Microscopy) with Airyscan® 2 detector in multiplex SR-4Y mode, through the cover glass.

For overviews of the cultures a long working distance 5x objective (C Epiplan-Apochromat 5x, NA 0.2, averaging 2x) was used to prepare z-stack images (voxel size: 0.247 x 0.247 x 10 µm). For higher resolution stacks, to allow for orientation analysis, the full culture or regions of interest were visualized using a 10x objective (C Epiplan-Apochromat 10x, NA 0.4, averaging 2x, voxel size: 0.124 x 0.124 x 1.420 µm). To perform high resolution imaging in a region of interest, a 63x water immersion objective (C-Apochromat 63x W.Corr, NA 1.2, averaging 2x, voxel size: 0.041 x 0.041 x 0.160 µm) was used to prepare z-stacks.

Live Raman microscopy

To prepare the microtissues for live Raman microscopy, the culture medium of unstained, living on-chip cultures was removed and replaced by OIM without phenol red (41061-029). Samples were transferred to the Raman microscope (WITec alpha 300R) and overview optical images were prepared with a 10x objective (NA 0.25). Regions of interest for a depth scan were selected in WITec Control Six (v6.1) software and depth scans were performed using a Zeiss 63x water immersion objective (C-Apochromat 63x W.Corr, NA 1.2) with excitation laser 457 nm at a laser power of 15 mW. Images were recorded with a resolution of 1 x 1 µm with exposure of 4 s per pixel. Recorded spectra were analyzed with WITec Project SIX software. Spectra were baseline corrected with the inbuilt shape correction (radius set at 400) and corrected for cosmic rays. True Component Analysis (TCA) was performed on the sample to identify the different chemical regions, spectra were normalized for the CH_2 vibration (~1450 cm^{-1}) and color images were created based on the recorded map and selected component.

Cryo-preservation of microtissues and cryo-fluorescence microscopy

After 42 days of differentiation, the cell cultures were extracted from the chips after live fluorescence microscopy using a skin biopsy punch (diameter 3 mm). The culture was removed from the pillars and transferred to a high pressure freezing carrier (Type A, diameter 3 mm, depth 100 µm, aluminium (M.Wohlwend, 241)) covered in 20% FCS in αMEM (phenol-red free), using a thin needle. The sample was then fluorescently imaged at the LSM900 upright, using a 5x objective (zoom 0.5, single plane), after which the carrier was closed with a flat surface carrier (type B, aluminium (M.Wohlwend, 242)) coated with phosphatidyl choline from egg yolk (1% w/v in ethanol (61755)) and preserved by high pressure freezing (HPM Live µ[15], CryoCapCell).

Samples were stored in liquid nitrogen until cryo-fluorescence microscopy. Cryo-fluorescence microscopy was performed on a LSM900 upright with Airyscan® 2 detector, using a Linkam LSM cryo-stage (CMS-196, Linkam Scientific Instruments). The sample was loaded into the cryo-holder (Art. 349559-8100-020, Zeiss cryo accessory kit) which was transferred to a Linkam adapter and imaged under cryogenic conditions to verify the sample location (10x objective, NA 0.4, zoom 0.5, z-steps = 1.42 µm). Afterward, the sample was stored again in liquid nitrogen until freeze substitution.

Automated Freeze Substitution and fluorescence microscopy of embedded samples

High-pressure frozen samples were placed in pre-cooled FS medium (0.1% Uranyl Acetate in 2.5% (v/v) H_2O in acetone, -90°C, 72 h) for automated freeze substitution (Leica Microsystems, AFS2). The temperature was gradually increased (3°C/h) to -45°C. After 5 h of incubation at -45°C, the FS medium was replaced by acetone in three sequential acetone incubation steps (10 min), followed by two ethanol incubations (10 min). After this dehydration procedure, a series of Lowicryl HM20 (10%-100%, Table 1) was used for embedding, while gradually increasing the temperature to -25°C (Table 1). The pure Lowicryl HM20 solution was then replaced two more times before fresh Lowicryl HM20 was added and UV irradiation (48 h) was started. Finally, the temperature was increased to 20°C during UV irradiation.

Table 1 – Lowicryl HM20 Incubation Scheme

T_{start}	T_{end}	Slope	Time	Solution
-45°C	-45°C	0°C/h	6 h	Lowicryl HM20 10%
-45°C	-45°C	0°C/h	6 h	Lowicryl HM20 25%
-45°C	-35°C	1.67°C/h	12 h	Lowicryl HM20 50%
-35°C	-25°C	1.67°C/h	16 h	Lowicryl HM20 75%
-25°C	-25°C	0°C/h	10 h	Lowicryl HM20 100%
-25°C	-25°C	0°C/h	10 h	Lowicryl HM20 100%
-25°C	-25°C	0°C/h	10 h	Lowicryl HM20 100%

-25°C	-25°C	0°C/h	48 h (+UV)	Lowicryl HM20 100%
-25°C	+20°C	5°C/h	9 h (+UV)	Lowicryl HM20 100%

After embedding in Lowicryl HM20, samples were released from the HPF carriers by dipping the embedded sample in liquid nitrogen. The irregular surface was smoothened by sectioning with a microtome, until the first layer of each sample was on the surface. Sequentially, the resin blocks were immersed in MilliQ (30 min, RT) for rehydration and imaged using a LSM900 upright with Airyscan® 2 detector in SR-4Y mode, to make overviews (10x, C Epiplan-Apochromat 10x, NA 0.4, voxel size: 0.312 x 0.312 x 1.42 µm) and high-resolution z-stacks (40x water-dipping, W Plan-Apochromat 40x, NA 1.0, voxel size: 0.049 x 0.049 x 0.260 µm). In parallel to fluorescence microscopy, reflection microscopy (confocal) was used to visualize the surface of the sample for correlation with the SEM top-view. Reflection images were recorded using the 640 nm excitation laser of the Zeiss LSM900 upright. Images were aligned using the Zen connect module in ZEN 3.7 software (Carl Zeiss Microscopy) to allow for sequential FIB/SEM imaging at the region of interest.

3D FIB/SEM

After fluorescence microscopy of the HM20 embedded sample, the sample was coated with a gold sputter coater (Edwards) and transferred to a Zeiss Crossbeam 550 FIB/SEM for volume imaging. Using a top-view, the fluorescence and electron microscopy images were aligned, by overlaying these images in Zen Connect (ZEN 3.7). At the regions of interest, Pt and C were sequentially deposited before a coarse trench was milled using a 30 kV/30 nA FIB probe and smoothened with a 30 kV/3 nA FIB probe. Parameters for serial sectioning imaging were set in Atlas 3D software (Atlas Engine v5.3.3) to allow imaging at a 5x5x5 nm voxel size (FOV 15x20 µm), using a 30 kV/700 pA probe for serial FIB milling. InLens secondary and backscattered (grid -876V) electron microscopy images were simultaneously recorded (line average n=1, dwell time 0.7x4 µs) using an acceleration voltage of 2.0 kV and a probe current of 30 pA. After imaging, the ESB and InLens data were exported from Atlas as a combined file, using a 0.3 ratio of Inlens/ESB.

Image analysis

Fluorescent images were analyzed using FIJI 1.54f[31] and ZEN 3.7 (Carl Zeiss Microscopy). Z-stacks were processed by preparing Maximum Intensity Projections (MIP) for quick visualization. Additionally, 3D representations and orthogonal views were used to visualize 3D information. OrientationJ Analysis[32] and Distribution[33] were performed on MIPs of 10x z-stacks to visualize cellular and collagen alignment. Overlays of fluorescence and electron microscopy top views were prepared in ZEN 3.7, using Zen Connect, to allow for the alignment of the imaging modalities. After export, FIB/SEM data were denoised in ZEN 3.7 (Total variation, strength 1). The denoised images were then enhanced by local contrast enhancement (CLAHE) in FIJI (block size 49, slope 2.0). Horizontal stripe artifacts were removed after these processing steps, using the FFT power spectrum of the image and invert FFT function in FIJI.

Chip compression & modeling

Before compression, bonded chips with a PDMS top layer of approximately 200 µm were filled with UV-curable glue (Byllux6308, Byla GmbH) mixed with Oil red O (O9755) for visualization. The filled chips were placed on the bottom part of a custom-made compression device (Supplementary Figure 1). This plastic holder contained one 14.7 N NdFeB magnet (Q-20-05-02-HN, Supermagnete) above which the coverslip of the chip was placed. Next, the holder was closed with a top part, containing a movable actuator with pins that aligned with the center of the culture chambers of the chips, which also contained one magnet of the same type. The distance between the top and bottom part of the compression device was tuned with two screws that extended from the top part to the bottom part. After fixation of the chip in the compression device, the stained glue was cured for 30 min using a Honle Bluepoint 2 easy cure (365 nm, 2x 900 s) and left to harden further under compression for 2 days. After disassembly of the compression device, the hardened glue inside the cell culture chambers retained their shapes adopted under compression and the hardened glue in the chips was imaged with confocal fluorescence microscopy from the coverslip side using a LSM900 upright (C Epiplan-Apochromat 10x, NA 0.4, z-step 1.42 µm, averaging 2x). The height of the compressed chambers was measured using an orthogonal view from the 3D microscopy images, which was taken between the pillars. In these images, the height of the fluorescent signal was measured at the thinnest point.

The magnetic force between the magnets of the actuation device was measured using a dynamometer. The magnets were separated by a stack of glass slides with different thicknesses and the dynamometer, attached to one of the

magnets, was gradually pulled away from the second magnet, until the pulled magnet detached from the stack. The thickness of this stack was measured using a caliper to determine the distance between the magnets. The force-distance curve was plotted using the distance data and the force at detachment.

The computational modeling of the compression was performed using Comsol Multiphysics (6.0.0.312). The geometry of one quadrant of the chip and the compressive tip were built (**Figure 5**), because the whole system had 2 symmetrical planes: parallel to XZ-plane and YZ-plane with both planes going through the centered symmetry line. The tip was assumed to be non-deformable (built-in material from Comsol library: steel AISI 4340) and the properties of the PDMS were set according to previously published characteristics (density: 1065 kg/m^3,[34] Young's modulus: 1.5 MPa,[35] Poisson's ratio: 0.495[36]). To set up the solid mechanics, the *hyperelastic node* was added, and the Mooney-Rivlin-5-parameter model was selected with the following parameter values in MPa: C10=-0.46701; C01=0.88163; C11=-3.91278; C20=1.54142; C02=3.11667 with a bulk modulus of 3 GPa.[37] *The contact node* was used with these contact pairs: tip's surface and the top of the PDMS layer, as well as the top and bottom surfaces of the chamber. The augmented Lagrangian method was chosen over the penalty method. *Symmetry nodes* were defined at these 2 planes: parallel to XZ-plane and YZ-plane. The *fixed constraint node* was assigned to the side-faces of the glass slide. The last node to be added was *boundary displacement* with the function z=-x assigned to the surface of the tip. The meshes were created with the focus on the contact surfaces between the PDMS block and the tip, whereas the other components could be treated with reduced coarser meshes. The solver chosen was auxiliary sweep from 0 to 1 with a step size of 0.1 for the parameter x; when x=0, the tip was in the initial top position, not touching the PDMS surface. When x=0.1, the tip was in the first contact the PDMS surface; when x=1, the tip had travelled the full depth of the chamber.

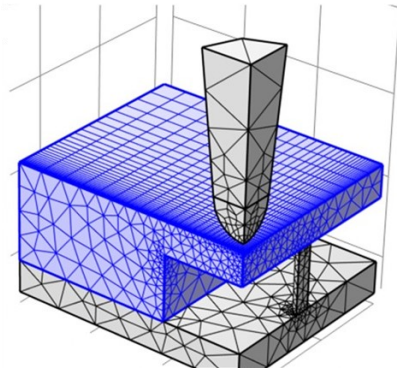

Figure 5 - Representation of Comsol Multiphysics model
Representation of one quadrant of the chip, as reconstructed in Comsol Multiphysics. The PDMS (in blue), compressive tip (grey to) and bottom glass slide (grey bottom) were included in the model.

Acknowledgements

The authors thank Harrie Weinans and Ralph Sakkers from University Medical Center Utrecht for providing the hMSCs. The authors also would like to thank Tom Boonen and Carla Cofiño-Fabres from the University of Twente for their help during the design phase of our device and for sharing their knowledge on OoC cell cultures in these types of devices, José Manuel Rivera Arbeleaz from the University of Twente for help with the modeling of the mechanical actuation, and Marcel de Bruine from University of Twente for 3D printing of the actuator parts. The project was supported by an European Research Council (ERC) Advanced Investigator grant (H2020-ERC-2017-ADV-788982-COLMIN) to N.S. A.A. was also supported by a VENI grant from the Netherlands Scientific Organization NWO (VI.Veni.192.094). N.S. and P.J. were supported by Growing bone-on-chip TURBO grant from University of Twente and Radboud University and P.J. was supported by Topconsortium voor Kennis en Innovatie (CHEMIE.PGT.2023.017) and an NWO-XL grant (OCENW.GROOT.2019.029).

References

[1] W. M. S. Russell, R. L. Burch, *The principles of humane experimental techniques*, Methuen & Co ltd, London **1959**.

[2] a) B. Zhang, A. Korolj, B. F. L. Lai, M. Radisic, *Nat. Rev. Mater.* **2018**, 3, 257; b) K. Ronaldson-Bouchard, G. Vunjak-Novakovic, *Cell Stem Cell* **2018**, 22, 310; c) S. N. Bhatia, D. E. Ingber, *Nat. Biotechnol.* **2014**, 32, 760; d) M. Rothbauer, J. M. Rosser, H. Zirath, P. Ertl, *Curr. Opin. Biotechnol.* **2019**, 55, 81.

[3] a) D. E. Ingber, *Nat. Rev. Genet.* **2022**, 23, 467; b) A. E. Danku, E. H. Dulf, C. Braicu, A. Jurj, I. Berindan-Neagoe, *Front. Bioeng. Biotechnol.* **2022**, 10, 840674; c) S. E. Park, A. Georgescu, D. Huh, *Science* **2019**, 364, 960.

[4] D. Huh, B. D. Matthews, A. Mammoto, M. Montoya-Zavala, H. Y. Hsin, D. E. Ingber, *Science* **2010**, 328, 1662.

[5] S. Jalili-Firoozinezhad, F. S. Gazzaniga, E. L. Calamari, D. M. Camacho, C. W. Fadel, A. Bein, B. Swenor, B. Nestor, M. J. Cronce, A. Tovaglieri, O. Levy, K. E. Gregory, D. T. Breault, J. M. S. Cabral, D. L. Kasper, R. Novak, D. E. Ingber, *Nat. Biomed. Eng.* **2019**, 3, 520.

[6] A. Marsano, C. Conficconi, M. Lemme, P. Occhetta, E. Gaudiello, E. Votta, G. Cerino, A. Redaelli, M. Rasponi, *Lab Chip* **2016**, 16, 599.

[7] a) C. M. Leung, P. de Haan, K. Ronaldson-Bouchard, G.-A. Kim, J. Ko, H. S. Rho, Z. Chen, P. Habibovic, N. L. Jeon, S. Takayama, M. L. Shuler, G. Vunjak-Novakovic, O. Frey, E. Verpoorte, Y.-C. Toh, *Nat. Rev. Methods Primers* **2022**, 2; b) M. Zommiti, N. Connil, A. Tahrioui, A. Groboillot, C. Barbey, Y. Konto-Ghiorghi, O. Lesouhaitier, S. Chevalier, M. G. J. Feuilloley, *Bioengineering (Basel)* **2022**, 9.

[8] S. Peel, M. Jackman, *Am. J. Physiol. Cell Physiol.* **2021**, 320, C669.

[9] a) A. Iordachescu, H. D. Amin, S. M. Rankin, R. L. Williams, C. Yapp, A. Bannerman, A. Pacureanu, O. Addison, P. A. Hulley, L. M. Grover, *Adv. Biosyst.* **2018**, 2, 1700156; b) A. Akiva, J. Melke, S. Ansari, N. Liv, R. Meijden, M. Erp, F. Zhao, M. Stout, W. H. Nijhuis, C. Heus, C. Muñiz Ortera, J. Fermie, J. Klumperman, K. Ito, N. Sommerdijk, S. Hofmann, *Adv. Funct. Mater.* **2021**, 31, 2010524; c) J. Sasaki, T. Matsumoto, S. Imazato, *Journal of Biomedical Materials Research Part A* **2015**, 103, 622; d) S. Kawai, J. Sunaga, S. Nagata, M. Nishio, M. Fukuda, T. Kamakura, L. Sun, Y. Jin, S. Sakamoto, A. Watanabe, S. Matsuda, T. Adachi, J. Toguchida, *Sci. Rep.* **2023**, 13, 1094.

[10] a) M. K. Kim, K. Paek, S.-M. Woo, J. A. Kim, *ACS Biomater. Sci. Eng.* **2023**, 9, 3058; b) S. Chen, X. Chen, Z. Geng, J. Su, *Bioact. Mater.* **2022**, 18, 15.

[11] a) N. Rosa, R. Simoes, F. D. Magalhaes, A. T. Marques, *Med. Eng. Phys.* **2015**, 37, 719; b) N. H. Hart, S. Nimphius, T. Rantalainen, A. Ireland, A. Siafarikas, *J. Musculoskelet. Neuronal Interact.* **2017**, 17; c) P. Katsimbri, *Eur. J. Cancer Care (Engl.)* **2017**, 26.

[12] a) Y. Park, E. Cheong, J.-G. Kwak, R. Carpenter, J.-H. Shim, J. Lee, *Sci. Adv.* **2021**, 7, eabd6495; b) S. K. O'Connor, D. B. Katz, S. J. Oswald, L. Groneck, F. Guilak, *Tissue Eng. Part A* **2021**, 27, 1099; c) A. Iordachescu, E. A. B. Hughes, S. Joseph, E. J. Hill, L. M. Grover, A. D. Metcalfe, *NPJ Microgravity* **2021**, 7, 17.

[13] a) S. Hao, G. Cheng, Y. Wan, Y. Xia, D. M. Sosnoski, A. M. Mastro, S. Y. Zheng, *Transducers* **2017**; b) G. Nasello, P. Alaman-Diez, J. Schiavi, M. A. Perez, L. McNamara, J. M. Garcia-Aznar, *Front. Bioeng. Biotechnol.* **2020**, 8, 336; c) A. Mansoorifar, R. Gordon, R. Bergan, L. E. Bertassoni, *Adv. Funct. Mater.* **2021**, 31; d) M. A. M. Vis, F. Zhao, E. S. R. Bodelier, C. M. Bood, J. Bulsink, M. van Doeselaar, H. E. Amirabadi, K. Ito, S. Hofmann, *Bone* **2023**, 173, 116812; e) H. Bahmaee, R. Owen, L. Boyle, C. M. Perrault, A. A. Garcia-Granada, G. C. Reilly, F. Claeyssens, *Front. Bioeng. Biotechnol.* **2020**, 8, 557111.

[14] a) J.-I. Sasaki, T. Matsumoto, H. Egusa, T. Nakano, T. Ishimoto, T. Sohmura, H. Yatani, *Soft Matter* **2010**, 6; b) N. de Jonge, F. M. Kanters, F. P. Baaijens, C. V. Bouten, *Ann. Biomed. Eng.* **2013**, 41, 763; c) G. Agrawal, A. Aung, S. Varghese, *Lab Chip* **2017**, 17, 3447; d) P. Bose, J. Eyckmans, T. D. Nguyen, C. S. Chen, D. H. Reich, *ACS Biomater. Sci. Eng.* **2019**, 5, 3843; e) C. Cofino-Fabres, T. Boonen, J. M. Rivera-Arbelaez, M. Rijpkema, L. Blauw, P. C. N. Rensen, V. Schwach, M. C. Ribeiro, R. Passier, *Adv. Healthc. Mater.* **2024**, DOI: 10.1002/adhm.202303664e2303664.

[15] X. Heiligenstein, M. de Beer, J. Heiligenstein, F. Eyraud, L. Manet, F. Schmitt, E. Lamers, J. Lindenau, M. Kea-Te Lindert, J. Salamero, G. Raposo, N. Sommerdijk, M. Belle, A. Akiva, *Methods Cell Biol.* **2021**, 162, 115.

[16] a) X. Heiligenstein, J. Heiligenstein, C. Delevoye, I. Hurbain, S. Bardin, P. Paul-Gilloteaux, L. Sengmanivong, G. Regnier, J. Salamero, C. Antony, G. Raposo, *Traffic* **2014**, 15, 700; b) E. Shimoni, M. Muller, *J. Microsc.* **1998**, 192, 236.

[17] H. Hanna, L. M. Mir, F. M. Andre, *Stem Cell. Res. Ther.* **2018**, 9, 203.

[18] a) N. Jaiswal, S. E. Haynesworth, A. I. Caplan, S. P. Bruder, *J. Cell. Biochem.* **1998**, 64, 295; b) H. C. Tenenbaum, *J. Dent. Res.* **1981**, 60, 1586; c) H. C. Tenenbaum, J. N. M. Heersche, *Calcif. Tissue Int.* **1982**, 34, 76.

[19] Z. Movasaghi, S. Rehman, I. U. Rehman, *Applied Spectroscopy Reviews* **2007**, 42, 493.

[20] E. Mailand, B. Li, J. Eyckmans, N. Bouklas, M. S. Sakar, *Biophys. J.* **2019**, 117, 975.

[21] K. Zha, Y. Tian, A. C. Panayi, B. Mi, G. Liu, *Front. Cell. Dev. Biol.* **2022**, 10, 824812.

[22] a) C. L. Gregg, J. T. Butcher, *Differentiation* **2012**, 84, 149; b) S. Iyer, S. Mukherjee, M. Kumar, *Bioessays* **2021**, 43, e2000238.

[23] B. Schamberger, S. Ehrig, T. Dechat, S. Spitzer, C. M. Bidan, P. Fratzl, J. W. C. Dunlop, A. Roschger, *PNAS Nexus* **2024**, 3.

[24] a) P. Fratzl, F. D. Fischer, G. A. Zickler, J. W. C. Dunlop, *PNAS Nexus* **2023**, 2, pgac292; b) S. Ehrig, B. Schamberger, C. M. Bidan, A. West, C. Jacobi, K. Lam, P. Kollmannsberger, A. Petersen, P. K. Tomancak, K. , F. D. Fischer, P. Fratzl, J. W. C. Dunlop, *Sci. Adv.* **2019**, 5, eaav9394.

[25] a) E. D'Imprima, M. Garcia Montero, S. Gawrzak, P. Ronchi, I. Zagoriy, Y. Schwab, M. Jechlinger, J. Mahamid, *Dev. Cell* **2023**, 58, 616; b) J. Jansen, K. C. Reimer, J. S. Nagai, F. S. Varghese, G. J. Overheul, M. de Beer, R. Roverts, D. Daviran, L. A. S. Fermin, B. Willemsen, M. Beukenboom, S. Djudjaj, S. von Stillfried, L. E. van Eijk, M.

Mastik, M. Bulthuis, W. D. Dunnen, H. van Goor, J. L. Hillebrands, S. H. Triana, T. Alexandrov, M. C. Timm, B. T. van den Berge, M. van den Broek, Q. Nlandu, J. Heijnert, E. M. J. Bindels, R. M. Hoogenboezem, F. Mooren, C. Kuppe, P. Miesen, K. Grunberg, T. Ijzermans, E. J. Steenbergen, J. Czogalla, M. F. Schreuder, N. Sommerdijk, A. Akiva, P. Boor, V. G. Puelles, J. Floege, T. B. Huber, C. M. consortium, R. P. van Rij, I. G. Costa, R. K. Schneider, B. Smeets, R. Kramann, *Cell Stem Cell* **2022**, 29, 217.

[26] I. Begemann, M. Galic, *Front. Synaptic Neurosci.* **2016**, 8, 28.

[27] N. Pien, H. Krzyslak, S. Shastry Kallaje, J. Van Meerssche, D. Mantovani, C. De Schauwer, P. Dubruel, S. Van Vlierberghe, C. P. Pennisi, *Appl. Mater. Today* **2023**, 31.

[28] a) B. J. Blackburn, M. W. Jenkins, A. M. Rollins, W. J. Dupps, *Front. Bioeng. Biotechnol.* **2019**, 7, 66; b) J.-M. Bourget, M. Guillemette, T. Veres, F. o. A. Auger, L. Germain, in *Advances in Biomaterials Science and Biomedical Applications*, DOI: 10.5772/54142 (Ed: P. Rosario), IntechOpen, Rijeka **2013**, p. Ch. 14.

[29] C. L. Thompson, S. Fu, M. M. Knight, S. D. Thorpe, *Front. Bioeng. Biotechnol.* **2020**, 8, 602646.

[30] a) S. J. Aper, A. C. van Spreeuwel, M. C. van Turnhout, A. J. van der Linden, P. A. Pieters, N. L. van der Zon, S. L. de la Rambelje, C. V. Bouten, M. Merkx, *PLoS One* **2014**, 9, e114983; b) K. N. Krahn, C. V. Bouten, S. van Tuijl, M. A. van Zandvoort, M. Merkx, *Anal. Biochem.* **2006**, 350, 177.

[31] J. Schindelin, I. Arganda-Carreras, E. Frise, V. Kaynig, M. Longair, T. Pietzsch, S. Preibisch, C. Rueden, S. Saalfeld, B. Schmid, J.-Y. Tinevez, D. J. White, V. Hartenstein, K. Eliceiri, P. Tomancak, A. Cardona, *Nat. Methods* **2012**, 9, 676.

[32] Z. Püspöki, M. Storath, D. Sage, M. Unser, *Adv. Anat. Embryol. Cell Biol.* **2016**, 219, 69.

[33] R. Rezakhaniha, A. Agianniotis, J. T. C. Schrauwen, A. Griffa, D. Sage, C. V. C. Bouten, F. N. van de Vosse, M. Unser, N. Stergiopulos, *Biomechanics and Modeling in Mechanobiology* **2012**, 11, 461.

[34] H. Hocheng, C.-M. Chen, Y.-C. Chou, C.-H. Lin, *Microsyst. Technol.* **2010**, 16, 423.

[35] a) E. Rubino, T. Ioppolo, *Journal of Polymer Science Part B: Polymer Physics* **2015**, 54, 747; b) I. D. Johnston, D. K. McCluskey, C. K. L. Tan, M. C. Tracey, *Journal of Micromechanics and Microengineering* **2014**, 24, 035017.

[36] A. Müller, M. C. Wapler, U. Wallrabe, *Soft Matter* **2019**, 15, 779.

[37] J. Phothiphatcha, T. Puttapitukporn, *Eng. J.* **2021**, 25, 11.